ELSEVIER

Journal of Fluids and Structures 19 (2004) 491–510

JOURNAL OF
FLUIDS AND
STRUCTURES

www.elsevier.nl/locate/jnlabr/yjfls

Vortex formation and force characteristics of a foil in the wake of a circular cylinder

Q. Liao, G.-J. Dong, X.-Y. Lu*

Department of Modern Mechanics, University of Science and Technology of China, Hefei, Anhui 230026, PR China

Received 3 October 2003; accepted 5 March 2004

Abstract

A numerical simulation is performed to investigate the vortex structure and force characteristics of a foil placed in the wake of a circular cylinder by solving the two-dimensional incompressible Navier–Stokes equations with a finite element method. The objective of this study is to reveal the vortex structures in the near region of the foil when the vortices shed from the circular cylinder are incident upon the foil, and to deal with the forces acting on the cylinder and the foil. Based on the relative position of the foil and the cylinder, three basic types of interference are classified; correspondingly, some basic patterns of vortex shedding are identified in the near region of the foil. According to our calculated results, it is found that a preferred vortex shedding frequency of the foil is synchronized with that of the cylinder due to the interference between the cylinder and the foil. Further, the influence of the relative position between the cylinder and foil and the incidence angle of the foil on the vortex formation, force character, and the frequency of the vortex shedding is analyzed and discussed.

1. Introduction

Viscous flow past a bluff body has received a great deal of attention, owing mainly to its theoretical and practical significance. In particular, the flow around a circular cylinder has been well studied and is one of the classical problems of fluid dynamics. In a variety of engineering applications and natural phenomena, vortex shedding is responsible for problems with flow-induced vibration and noise. A complete understanding of the fluid dynamics for the flow around a circular cylinder encompasses such fundamental subjects as the boundary layer, the free-shear layer, the wake and the dynamics of vortices. Therefore, a number of studies have been experimentally and numerically performed on the single-cylinder flow. However, viscous flow around two or more bluff bodies is less well studied and understood. In the following, the relevant work on flow past multiple cylinder configuration, in particular for multiple circular cylinders in uniform flow, is briefly reviewed.

The flow field of a multiple cylinder configuration involves complex interactions between the shear layers, vortices and Karman vortex streets [Zdravkovich (1977, 1987); Rockwell (1998)]. Recently, some investigations have provided more insight into the interference between circular cylinders, which, among various body shapes, has received the most research attention [Gu and Sun (1999); Sumner et al. (2000); Dalton et al. (2001); Zhou et al. (2001, 2002); Kang (2003); Keser and Unal (2003); Xu et al. (2003)]. As found in these studies, the flow structures are complex for flow around multiple cylinders. Thus, a classification of the flow behavior around multiple cylinders is needed.

---

*Corresponding author. Tel.: +86-551-3603223; fax: +86-551-3606459.
E-mail address: xlu@ustc.edu.cn (X.-Y. Lu).

0889-9746/$ - see front matter © 2004 Elsevier Ltd. All rights reserved.
doi:10.1016/j.jfluidstructs.2004.03.001

Some typical approaches have been used in an attempt to classify the flow behavior around multiple stationary circular cylinders. The simplest approach proposed by Zdravkovich (1987) is to classify the flow behavior into two basic types of interference based on the location of the downstream cylinder with respect to the upstream one. One is wake interference, when one of the cylinders is partially or completely submerged in the wake of the other, and the other is proximity interference, when the two cylinders are located close to one another, but neither is submerged in the wake of the other. Recently, Gu and Sun (1999) extended this classification to three different types, namely wake interference, shear layer interference, and neighborhood interference. Both these classifications, however, fail to recognize the complex behavior displayed in experiments and the wide range of flow patterns observed [Williamson (1985); Sumner et al. (2000)). The other approach is through the interpretation of experimental data; specifically, vortex shedding frequencies, and lift and drag forces (Zdravkovich (1977); Igarashi (1981, 1984)]. Such an approach is useful from an engineering design point of view, and has led to many recommendations for avoiding the occurrence of flow-induced vibration, for instance. However, determining the flow behavior from such measured quantities hardly provides an understanding of complex flow structures. A further approach to understanding the fluid dynamics of multiple cylinders is to identify the flow behavior based on flow visualization for the various flow patterns which arise for different choices of the geometry [Lam and Cheung (1988); Lam and Lo (1992); Sumner et al. (2000); Dalton et al. (2001); Lam et al. (2003)].

In this study, flow past a cylinder–foil configuration, where the foil is placed in the wake of the circular cylinder, is investigated. Previously, a stationary foil was employed as a vortex splitting device in boundary layer control Dowling (1985). Further, based on an active flow control concept, an oscillating foil was used as an effective approach in active vorticity control in a shear flow [Gopalkrishnan et al. (1994); Streitlien et al. (1996); Barrett et al. (1999); Triantafyllou et al. (2000)]. To the authors' knowledge, however, little work has been performed numerically to investigate the vortex structure and force character of the foil placed in the wake of the circular cylinder. According to these approaches, described above, to classify the flow behavior around multiple cylinders, some basic classifications are proposed, and the vortex formation, force character and the frequency of the vortex shedding are investigated. Here, three basic types of interference based on the relative position of the foil and the cylinder are classified and described as the foil placed inside the cylinder wake (ICW), on the edge of the cylinder wake (ECW), and outside the cylinder wake (OCW). Meanwhile, some typical flow patterns, corresponding to these classifications, are identified in the near region of the foil, as well as lift and drag forces acting on the cylinder and the foil and the frequencies of vortex shedding are examined.

This paper is organized as follows. The mathematical formulations are described in Section 2. The numerical method is given in Section 3. In Section 4, the vortex structures in the near wake of the foil, force character acting on the foil and the cylinder, and the frequency of the vortex shedding are discussed. Finally, concluding remarks are summarized in Section 5.

2. Mathematical formulations

Shown in Fig. 1 is the sketch of the configuration of a circular cylinder and a foil. In this study, the diameter of the cylinder is equal to the chord length of the foil. The two-dimensional incompressible Navier–Stokes equations with primitive variables are employed for the calculation. Here, the cylinder diameter D and the approach velocity U_∞ are

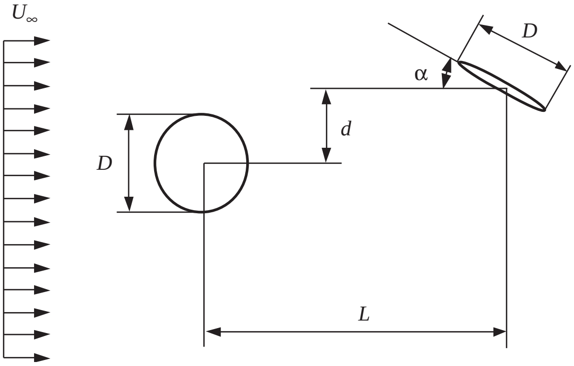

Fig. 1. Sketch of the configuration of a circular cylinder and a foil.

used as the length and velocity scales, respectively. Then the nondimensional incompressible Navier-Stokes equations are given as

$$\frac{\partial \vec{u}}{\partial t} + \vec{u} \cdot \nabla \vec{u} = -\nabla p + \frac{1}{\mathrm{Re}} \nabla^2 \vec{u} \tag{1}$$

$$\nabla \cdot \vec{u} = 0 \tag{2}$$

where $\vec{u}$ is the velocity vector, p is the pressure. The Reynolds number is defined as $\mathrm{Re} = U_\infty D/v$ with v being the kinematic viscosity.

No-slip and no-penetration velocity boundary conditions are used on the surfaces of the foil and the cylinder. A uniform velocity is set at the upstream far boundary, and a Neumann velocity boundary condition $\partial \vec{u}/\partial n_F = 0$ is employed at the downstream far boundary and along the upper and lower boundaries of the computational domain, where $\vec{n}_F$ indicates the unit vector in the boundary normal direction. On the exterior far boundary, a pressure condition $\partial p/\partial n_F = 0$ is prescribed.

3. Numerical methods

A fractional-step velocity correction method proposed by Kovacs and Kawahara (1991) is used to solve Eqs. (1) and (2). The discretized form can be obtained by splitting Eq. (1) into two substeps as

$$\hat{\vec{u}} = \vec{u}^n - \Delta t \left[-\frac{1}{\mathrm{Re}} \nabla^2 \vec{u}^n + (\vec{u}^n \cdot \nabla) \vec{u}^n \right], \tag{3}$$

$$\vec{u}^{n+1} = \hat{\vec{u}} - \Delta t \nabla p^{n+1}, \tag{4}$$

where $\hat{\vec{u}}$ is an intermediate velocity, Δt is the time-step, and superscripts n and $n+1$ represent the time level. In the splitting method, it is required that the velocity field $\vec{u}^{n+1}$ satisfies the incompressibility constraint,

$$\nabla \cdot \vec{u}^{n+1} = 0. \tag{5}$$

Incorporating the incompressibility constraint into Eq. (4), we finally arrive at a separately solvable elliptic equation for the pressure in the form,

$$\nabla^2 p^{n+1} = \frac{1}{\Delta t} \nabla \cdot \hat{\vec{u}}. \tag{6}$$

To solve the elliptic equation given in Eq. (6), a pressure boundary condition must be implemented. The pressure boundary condition may be taken as a key factor for solving the incompressible Navier–Stokes equations. According to a study on the pressure boundary conditions [Gresho and Sani (1987)], the condition on body's surfaces is given as

$$\frac{\partial p}{\partial n_B} = -\frac{1}{\mathrm{Re}} (\nabla \times \nabla \times \vec{u}) \cdot \vec{n}_B, \tag{7}$$

where $\vec{n}_B$ represents the unit vector in the body's surface normal direction.

The finite element spatial discretization is performed using the Galerkin weighted residual method. The discretized formulation was described by Kovacs and Kawahara (1991) in detail.

4. Results and discussion

To illustrate the computational procedure, as shown in Fig. 1, computational parameters are chosen as the transverse distance $d = -2$ to 2, the longitudinal distance $L = 3$ to 8, the incidence angle of the foil $\alpha = 0^\circ$ to 45°, the cylinder diameter and the airfoil chord length $D = 1$, and the Reynolds number $\mathrm{Re} = 500$. The foil is chosen as an elliptical shape with the thickness ratio 0.1.

The vortex sheet shedding behind the circular cylinder is unstable and evolves into a three-dimensional structure at $\mathrm{Re} = 500$ based on pervious work [Williamson (1988, 1996); Henderson (1997); Persillon and Braza (1998)]. As stated earlier, however, the present calculation will be two dimensional. We recognize the limitation of this approach, but still feel that the results will be of practical use in examining the vortex formation and force character of the foil in the wake of the circular cylinder. Based on recent work for flow around multiple cylinders [Gu and Sun (1999); Sumner et al. (2000); Dalton et al. (2001); Kang (2003); Keser and Unal (2003); Xu et al. (2003)], we do anticipate that the

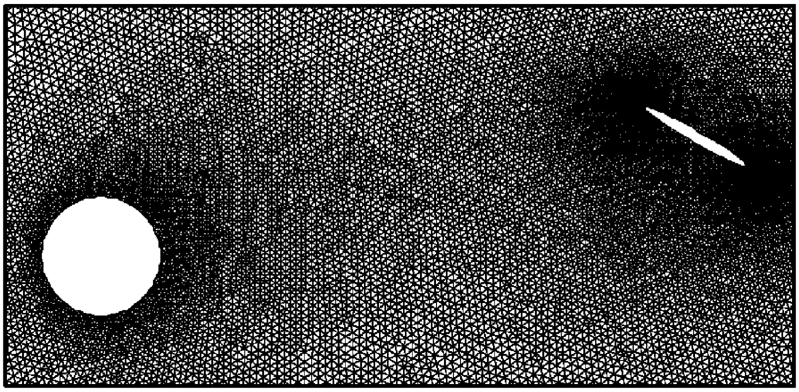

Fig. 2. Pattern of the unstructured mesh for the cylinder–foil configuration at $d = 1$, $L = 5$ and $\alpha = 30°$.

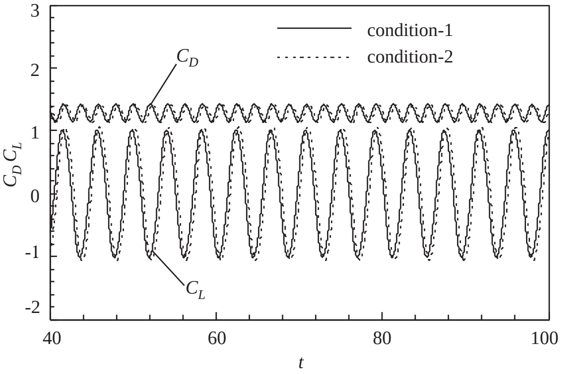

Fig. 3. Lift and drag coefficients for different grid resolutions and time steps at Re = 500. Condition(1): a number of elements $= 10^5$ and $\Delta t = 0.001$; condition(2): a number of elements 2×10^5 and $\Delta t = 0.0005$.

two-dimensional calculation can be used to reasonably predict and understand the large-scale vortex structures near the foil and force behaviors acting on the cylinder and the foil for the present problem.

To adapt the configuration of the cylinder and the foil with different relative positions and to increase the grid resolution near the bodies, an unstructured mesh is used in the finite element calculation. As a typical case, the local mesh near the bodies is shown in Fig. 2. Assuming a reference frame fixed with the circular cylinder with the origin of the frame at the center of the cylinder, the computational domain is from -10 to 35 along the longitudinal (or streamwise) direction (i.e., x-direction) and -15 to 15 along the transverse direction (i.e., y-direction). The number of elements for the present calculation is 10^5 approximately, and the time step is 0.001. It has been determined that the computed results are independent of the time step, the grid size and the computational domain size.

To demonstrate convergence of the solution, we compared two-grid systems: a number of elements$= 10^5$ approximately with Δt =0.001 and a number of elements $= 2 \times 10^5$ with Δt =0.0005 for the calculation of flow past individual circular cylinder at Re = 500. They produced virtually identical results as shown in Fig. 3; the only difference being a phase lag for the fine grid. The phase lag is attributed to the onset of the wake instability leading to vortex shedding. The Strouhal number (St), the time-average drag coefficient ($\bar{C}_D$), and the root-mean-square value of lift coefficient ($C_{L\mathrm{rms}}$), as determined from Fig. 3, are 0.23, 1.22 and 0.68, which compare well with the experimental data of approximately 0.22, 1.18 and 0.62, respectively, cited by Lu and Dalton (1996). The present computational code was also verified by our previous work [Lu et al. (2003); Shen et al. (2003); Wang et al. (2004)]. Thus, it can be confirmed that our calculation is reliable for the prediction of the formation and shedding of vortices from the cylinder and the foil. To further validate the present calculation for flow past both the cylinder and the foil, some quantitative comparisons will be given in the following section.

4.1. Force behavior and vortex structures in the near wake of the cylinder and the foil

One objective of this study is to investigate the vortex structures near the foil. Based on the transverse distance (d) between the cylinder and the foil, as shown in Fig. 1, three basic types of interference are classified for the foil placed inside the cylinder wake (ICW), on the edge of the cylinder wake (ECW) and outside the cylinder wake (OCW). Here, some calculated results for $L = 5$ and $\alpha = 30^\circ$ with different transverse distances are discussed to identify the vortex structures in the near wake of the cylinder and the foil.

4.1.1. Vortex structures for the type of the foil placed inside the cylinder wake (ICW)

Fig. 4 shows the time-dependent drag and lift coefficients (i.e., C_D and C_L) acting on the circular cylinder and the foil at $d = 0, L = 5$ and $\alpha = 30^\circ$, respectively. Based on the power spectrum density analysis of the lift coefficient, it is identified that the vortex shedding frequency of the foil is synchronized with that of the cylinder. Detailed discussion on the characteristics of the vortex shedding frequency will be given in the following section.

To illustrate the development of the vortex structures, Fig. 5 shows the instantaneous vorticity contours at $d = 0, L = 5$ and $\alpha = 30^\circ$. This case corresponds to the classification of ICW. As the vortices shed from the cylinder impinge on the foil, complex flow processes, including shear layer reattachment, induced separation, vortex pairing, and vortex impingement, are observed in the near region of the foil.

To clearly exhibit the vortex structures and to describe these processes in detail, Fig. 6 shows the time development of the vortex structures in the near region of the foil. In Figs. 6(a) and (b), a positive vortex V^C_{P1} shed from the cylinder is incident upon the foil, and a negative leading-edge vortex V^F_{L1} is generated from the foil, where the superscripts C and F represent the vortex shed from the cylinder and from the foil, respectively. Meanwhile, another leading-edge vortex V^F_{L0} formed previously is paired with a positive vortex V^C_{P0} to form a vortex-pair (i.e., $V^F_{L0} + V^C_{P0}$), and the vortex-pair is shed into the downstream region. Then, as shown in Figs. 6(c) and (d), the vortex V^C_{P1} interacts with the foil and induces shear layer reattachment along the lower-side of the foil, and the vortex V^F_{L1} is shed from the foil and moves into the

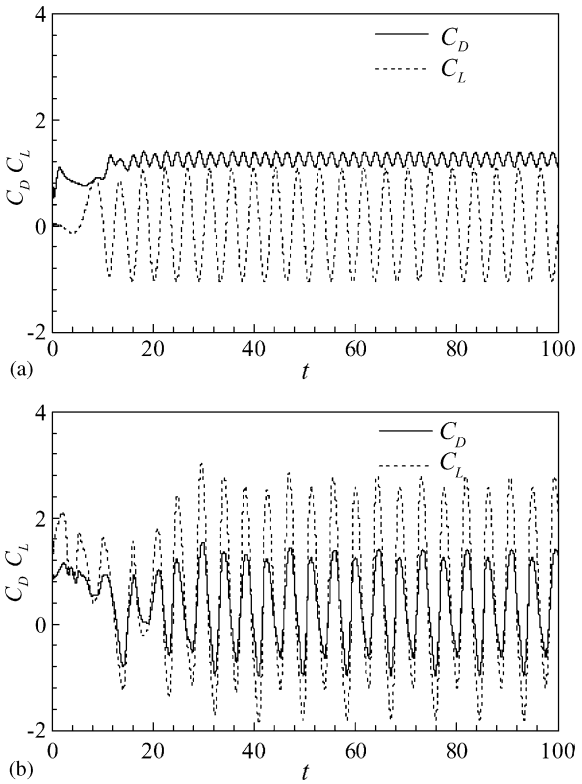

Fig. 4. Time-dependent drag and lift coefficients acting on the circular cylinder and the foil at $d = 0$, $L = 5$ and $\alpha = 30^\circ$: (a) cylinder; (b) foil.

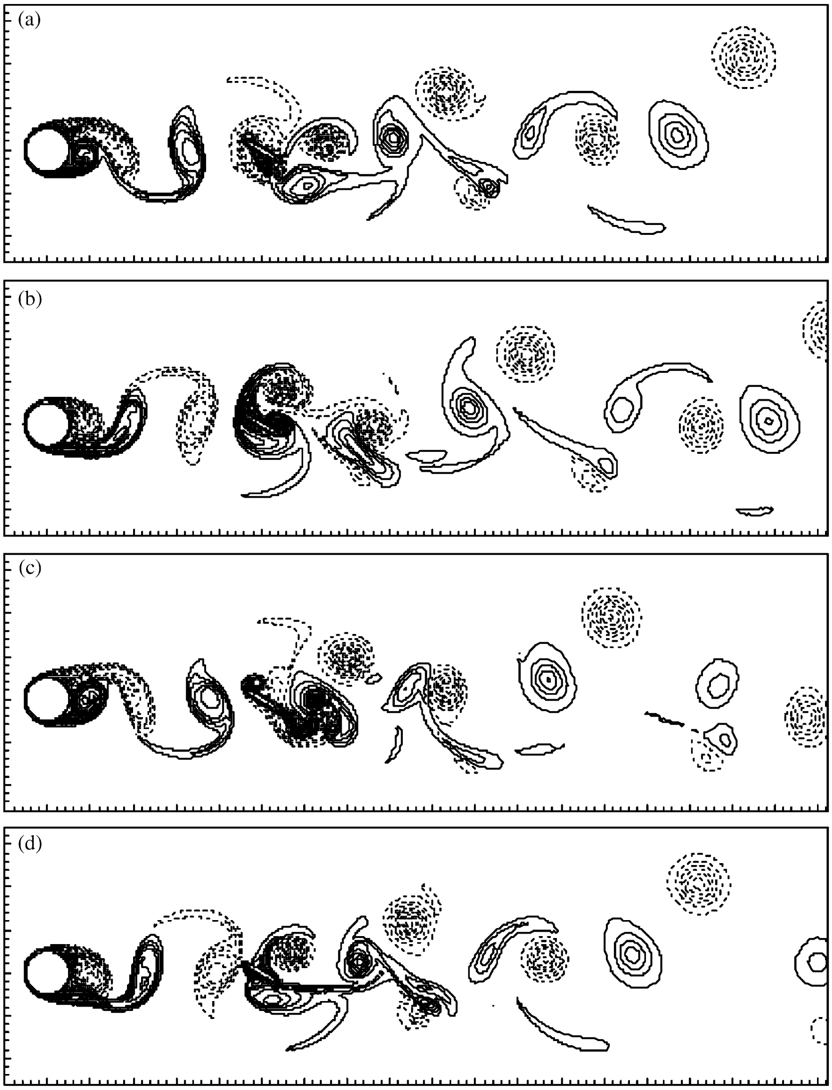

Fig. 5. Instantaneous vorticity contours at $d = 0, L = 5$ and $\alpha = 30°$: (a) $t = 90$; (b) 92.5; (c) 95; (d) 97.5.

downstream region. Meanwhile, a trailing-edge vortex V_{T1}^F is formed and connected with the vortex V_{P1}^C in Fig. 6(d), and a negative vortex V_{N1}^C impinges on the foil. In Figs. 6(e) and (f), the vortex V_{N1}^C interacts with the foil and induces a secondary vortex along the lower-side of the foil, and another positive vortex V_{P2}^C moves to the foil, and a negative leading-edge vortex V_{L2}^F is generated again. Further, both the vortices V_{T1}^F and V_{P1}^C in Figs. 6(g) and (h) are separated due to the interaction of the vortex V_{N1}^C and shed into the downstream region. Finally, as shown in Figs. 6(i) and 6(j), the vortex V_{P2}^C passes over the foil, another negative vortex V_{N2}^C interacts with the foil, and the vortex V_{L2}^F is shed into the downstream region. By comparing Figs. 6(j) with (a), the vortices V_{P3}^C, V_{N2}^C, V_{P2}^C, V_{L2}^F and V_{T1}^F in Fig. 6(j) correspond to V_{P1}^C, V_{N0}^C, V_{P0}^C, V_{L0}^F and V_{T0}^F in Fig. 6(a), respectively. In the following period, the vortex evolution is repeated as the above description, and the vortex structures formed in the downstream of the foil are shown in Fig. 5.

Some typical cases for the transverse distance d from -0.5 to 0.5 at $\alpha = 30°$, which belong to the case of the ICW, are also calculated. It is found that the development of the vortex structures (not shown here) is similar to that shown in Figs. 5 and 6.

4.1.2. *Vortex structures for the type of the foil placed on the edge of the cylinder wake (ECW)*

Fig. 7 shows the time-dependent drag and lift coefficients acting on the foil at $d = -1$ and 1 with $L = 5$ and $\alpha = 30°$. The drag and lift coefficients exhibit a periodic change with time. Meanwhile, based on the variation of the drag and lift

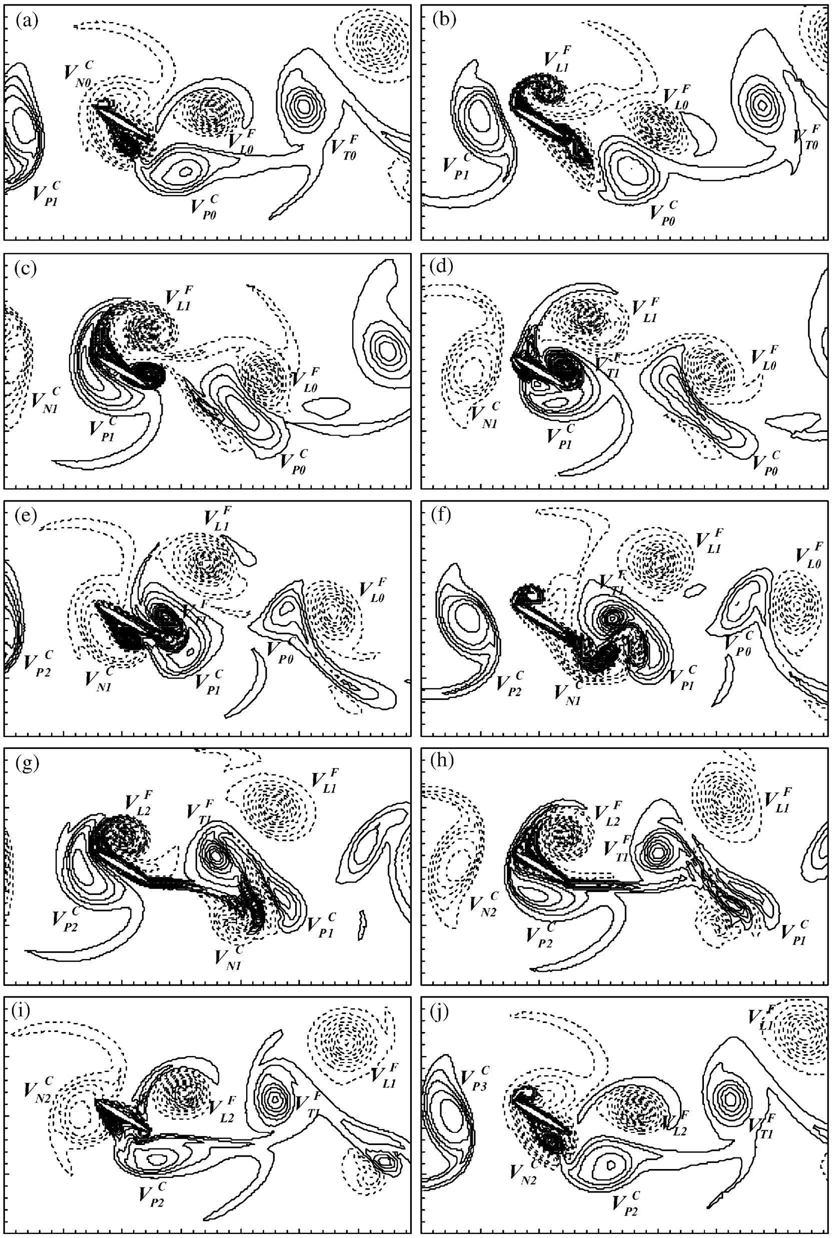

Fig. 6. Time development of the vortex structures in the near region of the foil at $d = 0$, $L = 5$ and $\alpha = 30°$: (a) t =90; (b) 91; (c) 92; (d) 93; (e) 94; (f) 95; (g) 96; (h) 97; (i) 98; (j) 99.

coefficients, it is found that the vortex shedding frequency of the foil is synchronized with that of the cylinder, due to the interaction of the vortices shed from the cylinder with the foil. Further, to demonstrate that the computed results are independent of the time steps and the grid sizes for flow past the cylinder and the foil, the results calculated by different grid numbers and time steps are shown in Figs. 7(a) and (b). These results are virtually identical; the only difference being a phase lag for the fine grid. Similar to Fig. 3 for flow past individual cylinder, the phase lag is attributed to the onset of the wake instability leading to vortex shedding.

To exhibit the flow structures in the downstream of the foil, Fig. 8 shows the instantaneous vorticity contours at $d = -1$ and 1 with $L = 5$ and $\alpha = 30^{\circ}$. Note that both the cases with $d = -1$ and 1 belong to the classification of ECW. The vortex structures demonstrate a row of vortex-pair plus a row of single vortices. In Fig. 8(a) at $d = -1$, the vortex

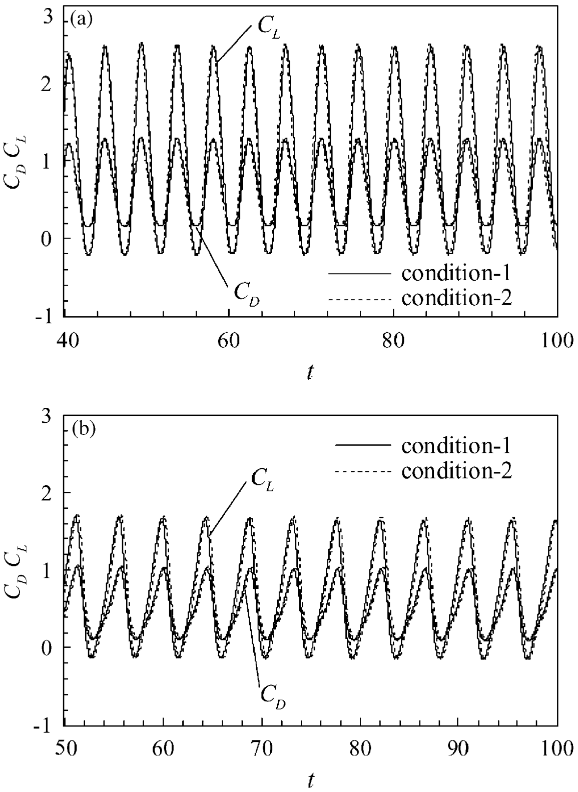

Fig. 7. Time-dependent drag and lift coefficients acting on the foil at $L = 5$ and $\alpha = 30°$: (a) $d = -1$; (b) $d = 1$. Condition1: a number of elements= 10^5 and Δt =0.001; condition2: a number of elements = 2×10^5 and Δt =0.0005.

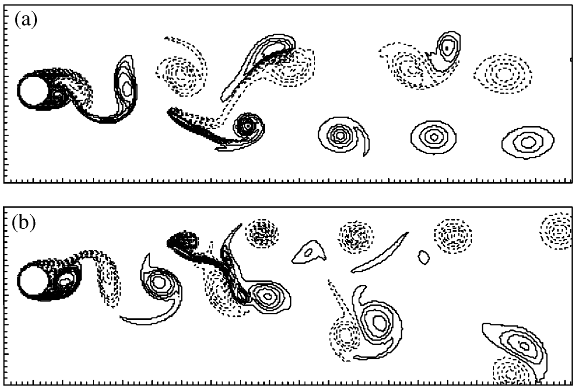

Fig. 8. Instantaneous vorticity contours at $L = 5$ and $\alpha = 30°$: (a) $d = -1$; (b) $d = 1$.

structures are a vortex-pair array over a single positive-vortex array; both the arrays are aligned in almost parallel arrangement in the near wake. Correspondingly, the vortex structures in Fig. 8(b) at $d = 1$ are a row of single vortices with negative rotation over a row of vortex-pairs; the vortex-pairs are induced to move downward because of the interaction with each of the vortices with opposite signs. The similar vortex structures were also found experimentally by Williamson and Roshko (1988) and Ongoren and Rockwell (1988) for approach flow past a transversely oscillating cylinder, and computationally by Lu and Dalton (1996), Lu and Sato (1996), Lu et al. (1997) and Lu (2002) for flow past a rotary oscillating cylinder and past a transversely oscillating cylinder, respectively.

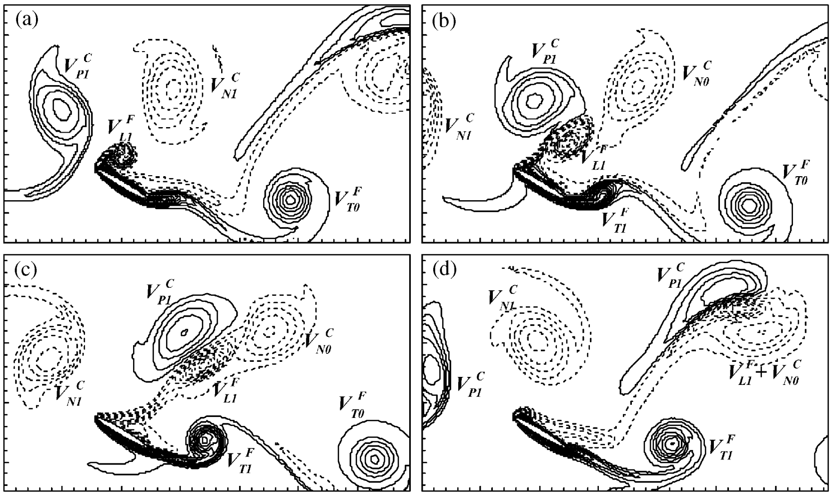

Fig. 9. Time development of the vortex structures in the near region of the foil at $d = -1$, $L = 5$ and $\alpha = 30°$: (a) $t = 90$; (b) 91; (c) 92; (d) 93.

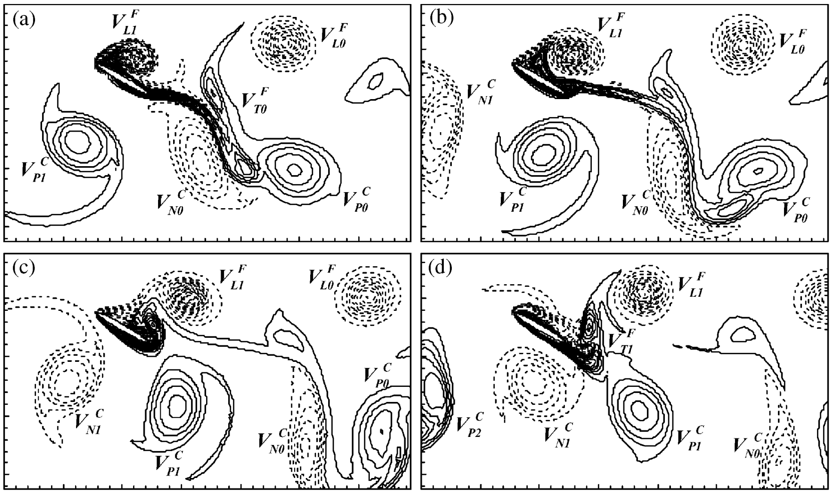

Fig. 10. Time development of the vortex structures in the near region of the foil at $d = 1$, $L = 5$ and $\alpha = 30°$: (a) $t = 90$; (b) 91; (c) 92; (d) 93.

Further, Fig. 9 shows the vortex structures in the near region of the foil at $d = -1$. In Fig. 9(a), a positive vortex V_{P1}^{C} is incident upon the foil, and a negative leading-edge vortex V_{L1}^{F} is generated. Meanwhile, another negative vortex V_{N0}^{C} stays over the vortex V_{L1}^{F}, and a positive trailing-edge vortex V_{T0}^{F} formed previously is shed downstream. In Figs. 9(b) and (c), the vortex V_{L1}^{F} strengthens and coalesces with the vortex V_{N0}^{C} to form a combined vortex $[V_{L1}^{F} + V_{N0}^{C}]$. Then, a negative vortex V_{N1}^{C} approaches the foil and a positive trailing-edge vortex V_{T1}^{F} is generated, as shown in Fig. 9(c). Finally, the vortex V_{P1}^{C} is paired with the combined vortex $[V_{L1}^{F} + V_{N0}^{C}]$ to form a vortex-pair (i.e., $V_{P1}^{C} + [V_{L1}^{F} + V_{N0}^{C}]$) and the vortex V_{T1}^{F} is shed into the downstream region. The vortex-pair and the vortex V_{T1}^{F} finally form the vortex-pair array and the single positive vortex array, as shown in Fig. 8(a). It is easy to get the corresponding relation of the vortices depicted in Figs. 9(a) and (d), and the vortex evolution is then repeated as the above description.

Fig. 10 demonstrates the instantaneous vorticity contours at $d = 1$. In Figs. 10(a) and (b), both vortices with opposite signs V_{P1}^{C} and V_{N1}^{C} impinge on the foil, a negative leading-edge vortex V_{L1}^{F} is generated. Meanwhile, a positive vortex V_{P0}^{C} shed previously coalesces with the trailing-edge vortex V_{T0}^{F} in Fig. 10(b) and is paired with the vortex V_{N0}^{C} to form a vortex-pair (i.e., $V_{P0}^{C} + V_{N0}^{C}$) in Fig. 10(c) The vortex-pair $V_{P0}^{C} + V_{N0}^{C}$ is shed downstream, and the vortices V_{P1}^{C} and V_{N1}^{C}

develop finally to form another vortex-pair (i.e., $V_{P1}^{C}+V_{N1}^{C}$). As shown in Fig. 10(d), the vortex V_{L1}^{F} moves downstream and a positive trailing-edge vortex V_{T1}^{F} is gradually generated. Finally, the vortex V_{T1}^{F} and the vortex-pair $V_{P1}^{C}+V_{N1}^{C}$ form the vortex patterns with a row of single vortex coupled with a row of vortex-pair, as shown in Fig. 8(b).

4.1.3. Vortex structures for the type of the foil placed outside the cylinder wake (OCW)

Fig. 11 shows the time-dependent drag and lift coefficients at $d=2, L=5$ and $\alpha=30^{\circ}$, which corresponds to the classification of OCW. Note that the influence between the cylinder and the foil still needs to be considered in this case. Based on our calculation test, for $|d|>8$ approximately, the interference effect between the cylinder and the foil may be negligibly small. To demonstrate the influence of the cylinder on the foil, it is noted that the vortex shedding frequency of the foil is synchronized with that of the cylinder based on the power spectrum density analysis of the lift coefficients.

Fig. 12 illustrates the instantaneous vorticity contours at $d=2$, $L=5$ and $\alpha=30^{\circ}$. The vortex structures in the near wake consist of the vortex-pair array generated from the foil and vortices array, similar to classic Karman vortex street, shed from the cylinder. During the evolution of the vortex structures, a shear layer generated from the foil rolls up to form another small-scale vortex, which is then mixed with the Karman vortex street.

4.2. Effect of the longitudinal distance L and the incidence angle α on vortex structures

To demonstrate the effect of the longitudinal distance (L) and the incidence angle of the foil (α) on the vortex structures in the near wake of the cylinder and the foil, some typical results are discussed for L =3 to 8 and $\alpha=0^{\circ}$ to 45°. As a typical case at $\alpha=0^{\circ}$, the vortex patterns with different transverse distances (d) are also exhibited in detail.

4.2.1. Vortex structures for different longitudinal spaces (L)

Fig. 13 shows the time-dependent drag and lift coefficients acting on the foil at $L=3$ and 8 with $d=0$ and $\alpha=30^{\circ}$. By comparing with the behavior of the drag and lift coefficients acting on the cylinder, the vortex shedding frequency of the foil is synchronized with that of the cylinder for $L=3$ and 8. Note that the vortex shedding frequency changes with the longitudinal distance and will be discussed in Section 4.4.

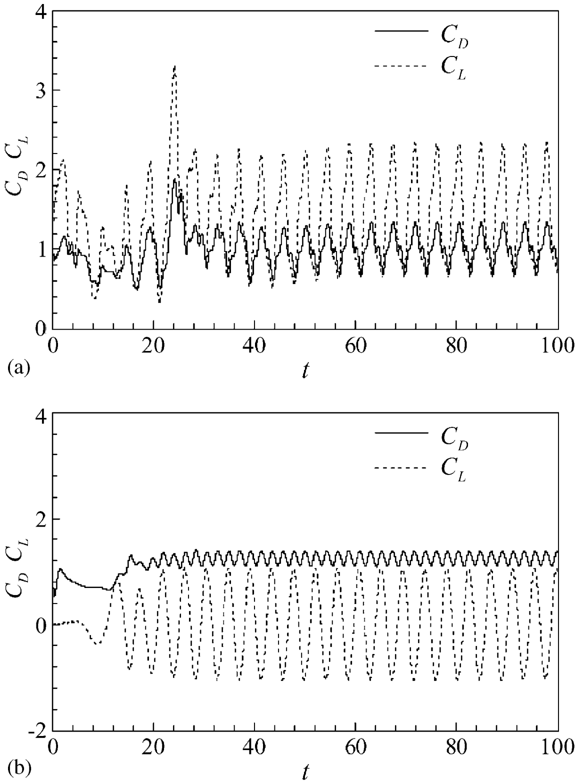

Fig. 11. Time-dependent drag and lift coefficients acting on the cylinder and the foil at $d=2, L=5$ and $\alpha=30°$: (a) foil; (b) cylinder.

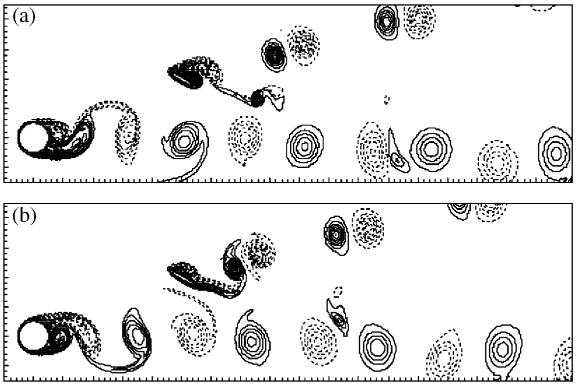

Fig. 12. Instantaneous vorticity contours at $d = 2$, $L = 5$ and $\alpha = 30°$. (a) $t = 92.5$; (b) 95.

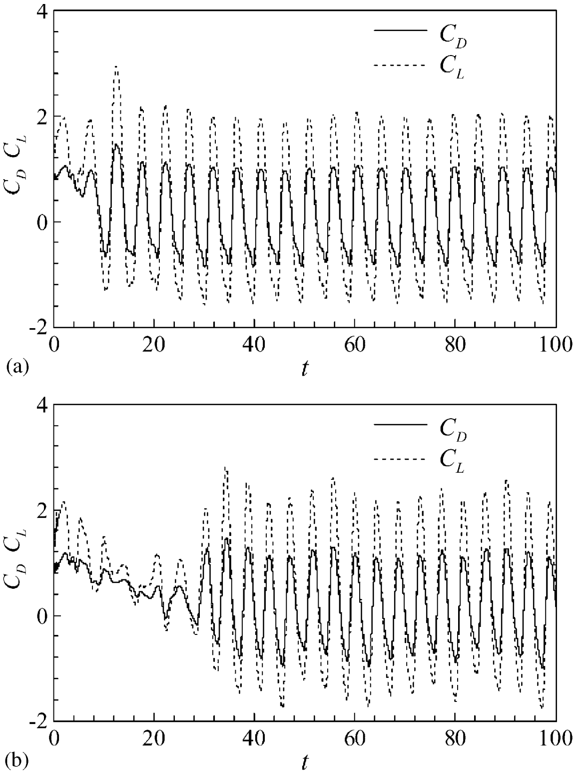

Fig. 13. Time-dependent drag and lift coefficients acting on the foil at $d = 0$ and $\alpha = 30°$: (a) $L = 3$; (b) $L = 8$.

The corresponding vorticity contours for $L = 3$ and 8 are shown in Figs. 14(a) and (b), respectively. When the Karman vortex street shed from the cylinder impinges on the foil, complex vortex patterns around the foil are observed. By observing the evolution of the vortex structures in the near region of the foil, the process for $L = 8$ is similar to that, as shown in Figs. 5 and 6, for $L = 5$. However, a somewhat different vortex structure development for $L = 3$ appears due to the proximity interference between the cylinder and the foil.

4.2.2. *Vortex structures for different incidence angles (α)*

Fig. 15 shows the time-dependent drag and lift coefficients acting on the foil at $\alpha = 15^{\circ}$ and 45° with $d = 0, L = 5$. The corresponding curves at $\alpha = 30^{\circ}$ are shown in Fig. 4b. The curves of the drag and lift coefficients change quasi-periodically with time. By calculating the vortex shedding frequencies of the cylinder and the foil, it is still found that the vortex shedding frequency of the foil is same as that of the cylinder at $\alpha = 15^{\circ}$ and 45°.

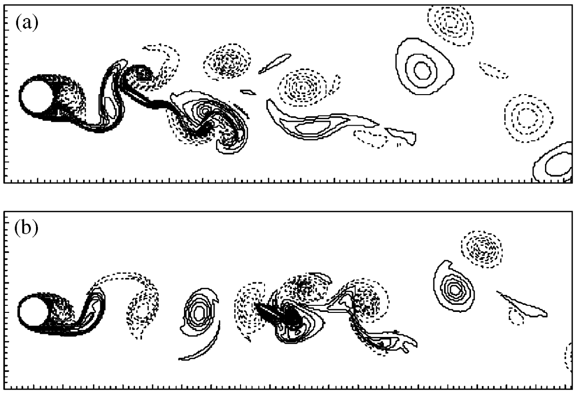

Fig. 14. Instantaneous vorticity contours at $d = 0$ and $\alpha = 30°$: (a) $L = 3$; (b) $L = 8$.

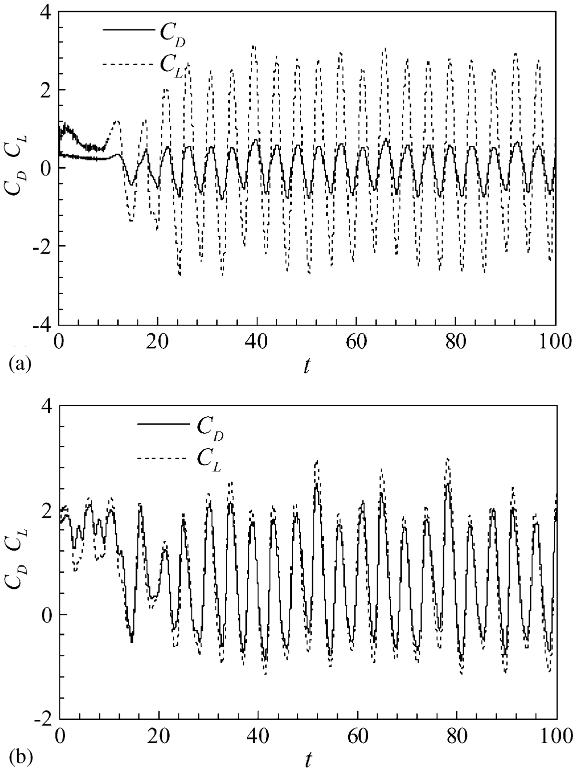

Fig. 15. Time-dependent drag and lift coefficients acting on the foil at $d = 0$ and $L = 5$: (a) $\alpha = 30°$; (b) $\alpha = 45°$.

The corresponding vorticity contours for $\alpha = 15^{\circ}$ and 45° are shown in Figs. 16(a) and (b), respectively. Basically, the evolution of the vortex structures in the near region of the foil at $\alpha = 15^{\circ}$ and 45° is similar to that at $\alpha = 30^{\circ}$, as shown in Figs. 5 and 6. By observing the flow patterns around the foil, the processes of vortex impingement, shear layer reattachment, induced separation, and vortex pairing are found.

4.2.3. Vortex structures at $\alpha = 0^{\circ}$

To understand the effect of the cylinder wake on vortex structures around the foil at $\alpha = 0^{\circ}$, Fig. 17 shows the vorticity patterns for $d = 0$, 1 and 2 with $L = 5$, respectively. In Fig. 17(a) for d=0, corresponding to the classification ICW, similar to Figs. 5 and 6 at $d = 0$ and α=30°, complex evolution of the vortex structures near the foil are observed. As d increases, as shown in Fig. 17(b) for $d = 1$ (i.e., the classification of ECW), the interference of vortices shed from

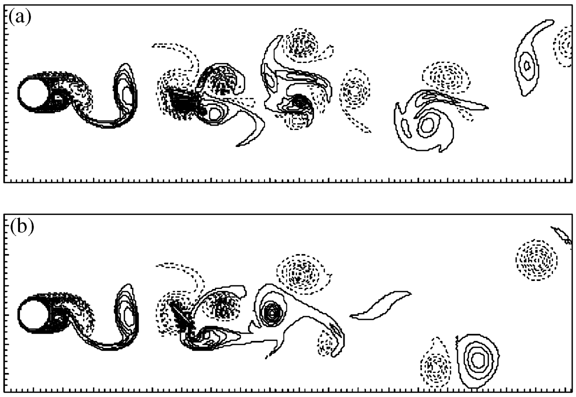

Fig. 16. Instantaneous vorticity contours at $d = 0$ and $L = 5$: (a) $\alpha = 15°$; ; (b) $\alpha = 45°$.

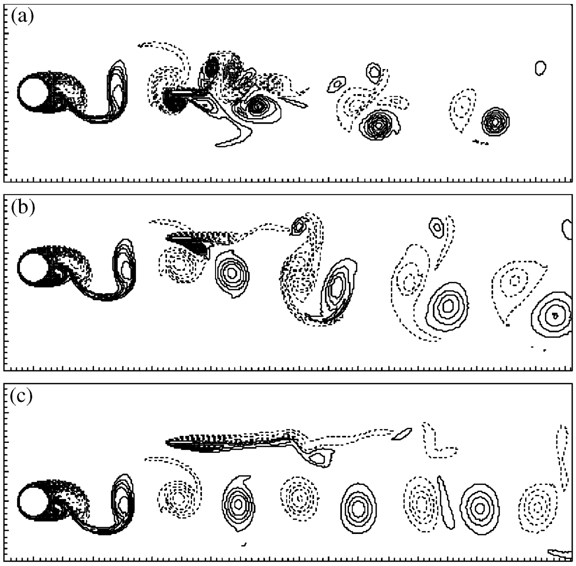

Fig. 17. Instantaneous vorticity patterns at $\alpha = 0°$ and $L = 5$: (a) $d = 0$; (b) $d = 1$; (c) $d = 2$.

the cylinder and from the foil appears. Further, in Fig. 17(c) for $d = 2$ (i.e., the classification of OCW), shear layers shed from the foil rollup to form small-scale vortices which are then mixed with the Karman vortex street shed from the cylinder.

4.3. Force characteristics

Due to the interference between the cylinder wake and the foil, the force behavior acting on the foil may vary with the transverse distance (d), the longitudinal distance (L) and the incidence angle of the foil (α). As described earlier, the time-dependent drag and lift coefficients acting on the foil are exhibited for some typical cases. Here, we are mainly concerned about the force characteristics acting on the foil; the time-mean drag and lift coefficients (i.e., $\bar{C}_D$ and $\bar{C}_L$) as well as their root-mean-square values (i.e., $C_{D\mathrm{rms}}$ and $C_{L\mathrm{rms}}$) are analyzed.

Fig. 18 shows the profiles of $\bar{C}_D, \bar{C}_L, C_{D\mathrm{rms}}$ and $C_{L\mathrm{rms}}$ versus d at $L = 5$ and $\alpha = 30^{\circ}$. As depicted in Fig. 18(a), the distributions of $\bar{C}_D, \bar{C}_L$ are concave upwards with small values during $d = -0.75 \sim 0.75$ which corresponds approximately to the region of the classification of ICW. With the increase of the absolute value of $d, \bar{C}_D$ and $\bar{C}_L$

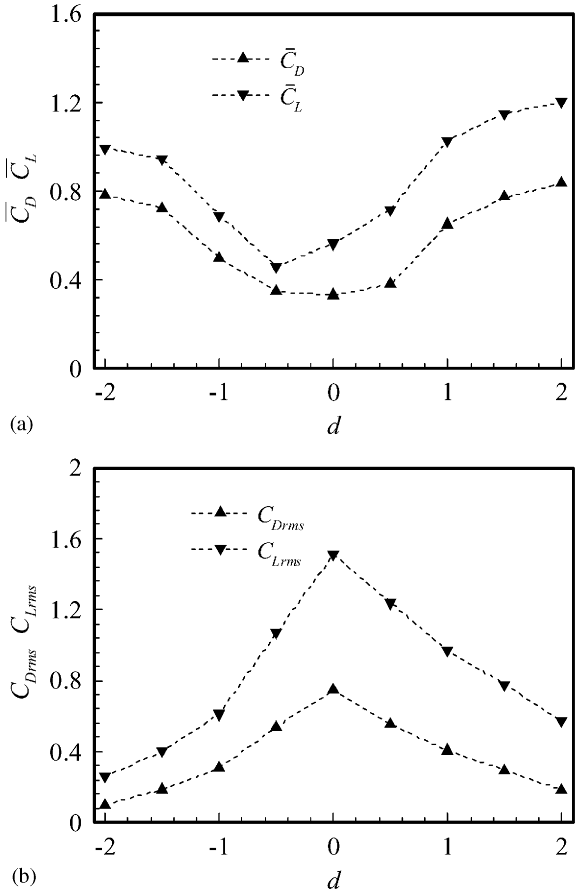

Fig. 18. Profiles of $\bar{C}_D, \bar{C}_L, C_{D\mathrm{rms}}$ and $C_{L\mathrm{rms}}$ versus d at $L=5$ and $\alpha=30°$: (a) $\bar{C}_D$ and $\bar{C}_L$; (b) $C_{D\mathrm{rms}}$ and $C_{L\mathrm{rms}}$.

approach the corresponding values for flow past individual foil at $\alpha = 30^\circ$. The values of $\bar{C}_D$ and $\overline{C}_L$ for the classification ICW are small with respect to those for uniform flow past the foil at the same incidence angle. The corresponding distributions of $C_{D\mathrm{rms}}$ and $C_{L\mathrm{rms}}$ as a function of d are exhibited in Fig. 18b. Both $C_{D\mathrm{rms}}$ and $C_{L\mathrm{rms}}$ approach peak values at $d = 0$ and decrease with the increase of the absolute value of d. This behavior is consistent with the finding for flow-induced vibration [e.g. Rockwell (1998)]. Meanwhile, based on the evolution of the vortex structures around the foil as shown in Figs. 5 and 6, it can be understood that the impingement of the vortex street shed from the cylinder induces a significant change of the force on the foil.

Fig. 19 exhibits the profiles of $\bar{C}_D, \bar{C}_L, C_{D\mathrm{rms}}$ and $C_{L\mathrm{rms}}$ versus L at $d = 0$ and $\alpha = 30^\circ$. The distributions of $\bar{C}_D$ and $\bar{C}_L$ are shown in Fig. 19(a), and are noted to peak at $L = 5$, and then decreases gradually with the increase of L. In Fig. 19(b), the values of $C_{D\mathrm{rms}}$ and $C_{L\mathrm{rms}}$ vary smoothly with L, and somewhat higher values of $C_{D\mathrm{rms}}$ and $C_{L\mathrm{rms}}$ appear for the region of $L = 4$–6. As the force behavior is closely related to the vortex structures near the foil, the primary vortex shed from the cylinder necessarily needs to develop and to then undergo strengthening in the near wake [Henderson (1997); Persillon and Braza (1998)]. Based on the spatial distribution of mean velocity along the rear axis of the cylinder given by Persillon and Braza (1998), it was noted that the maximum mean velocity, i.e. corresponding to the minimum deficit velocity, in the near wake of the cylinder appears at $L = 4.5$–5 for $\mathrm{Re} = 200$ and 300. Thus, it is reasonably predicted that the location of the peak values of $\bar{C}_D$ and $\bar{C}_L$ is about $L = 5$ as shown in Fig. 19(a).

Based on the time-dependent drag and lift coefficients acting on the foil in Figs. 4 and 15 for different incidence angles of the foil, the distributions of $\bar{C}_D, \bar{C}_L, C_{D\mathrm{rms}}$ and $C_{L\mathrm{rms}}$ versus α at $L = 5$ and $d = 0$ are given in Fig. 20. As α increases during the range of α considered here, $\bar{C}_D, \bar{C}_L$ and $C_{D\mathrm{rms}}$ increase and $C_{L\mathrm{rms}}$ decreases. Similar behavior was also found for flow control on an airfoil at large incidence angle Wu et al. (1998). As the foil shape is symmetrical, the drag and lift coefficients as well as their fluctuations reasonably approach together at $\alpha = 45^\circ$. Thus, as shown in Fig. 20, when $\alpha < 45^\circ$, both $\bar{C}_L$ and $C_{L\mathrm{rms}}$ have larger values with respect to $\bar{C}_D$ and $C_{D\mathrm{rms}}$ for the same α.

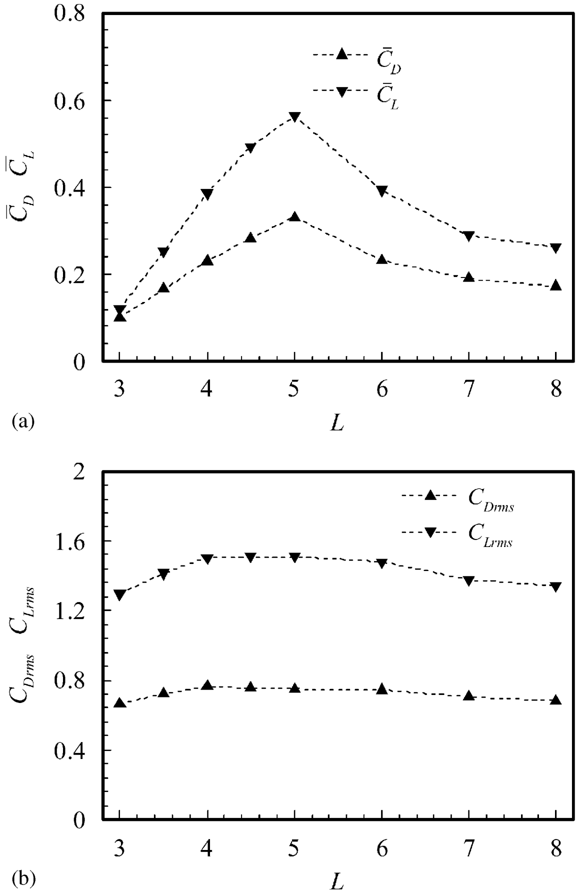

Fig. 19. Profiles of $\bar{C}_D, \bar{C}_L, C_{D\mathrm{rms}}$ and $C_{L\mathrm{rms}}$ versus L at $d = 0$ and $\alpha = 30°$: (a) $\bar{C}_D$ and $\bar{C}_L$; (b) $C_{D\mathrm{rms}}$ and $C_{L\mathrm{rms}}$.

Further, to understand the effect of the cylinder wake on the force behavior for the foil at $\alpha = 0^\circ$, Fig. 21 shows the profiles of $\bar{C}_D, \bar{C}_L, C_{D\mathrm{rms}}$ and $C_{L\mathrm{rms}}$ versus d at $L = 5$. By viewing Fig. 21(a), in particular for $\bar{C}_D$, it is interesting to find that $\bar{C}_D$ exhibits a small negative value for $d = -0.5$ to 0.5; a negative value of $\bar{C}_D$ corresponds to a thrust on the foil toward the cylinder. This behavior is reasonably consistent with the profile of $\bar{C}_D$ in Fig. 18(a) at $\alpha = 30^\circ$ with smaller value of $\bar{C}_D$ for $d = -0.75$ to 0.75. It is seen that $\bar{C}_D$ and $C_{D\mathrm{rms}}$ vary smoothly with d. Due to the velocity deficit induced by the wake effect, $\bar{C}_L$ is negative for $d<0$ and positive for $d > 0$. The distribution of $\bar{C}_L$ for $d \geq 0$ is exhibited to peak at $d = 0.5$ and then decreases as d increases. As expected, the profile of $C_{L\mathrm{rms}}$ exhibits a peak at $d = 0$.

As is well known, knowledge of the forces induced by incident vortices is central not only to flow-induced vibration and noise generation, but also to a remarkable concept of foil propulsion [Gopalkrishnan et al. (1994); Streitlien et al. (1996); Barrett et al. (1999)]. In the latter, when an incident vortex street approaches upon a foil subjected to controlled heaving and pitching motions, the foil may obtained the maximum efficiency, defined in terms of the normalized thrust [Streitlien et al. (1996); Barrett et al., (1999)]. As indicated by Rockwell (1998), this character is relevant to that the energy in an array of vortices can be exploited to enhance propulsive efficiency. Based on our calculated results shown in Fig. 21(a), a fixed foil under the interaction of an incident vortex street also exhibits the similar behavior disclosed by Streitlien et al. (1996) and Barrett et al. (1999).

4.4. Frequency selection

Usually, frequency selection of the vortex shedding is a critical problem in bluff body flows [Karniadakis and Triantafyllou (1989)]. Due to the interference between the cylinder and the foil, the changes of the vortex formation processes and the vortex shedding frequencies from the cylinder and the foil occur. When a vortex street shed from the

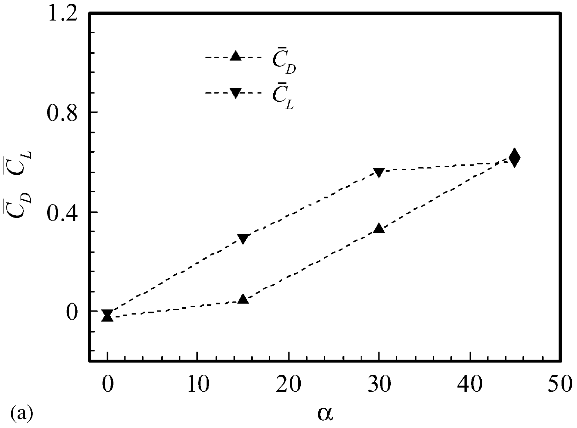

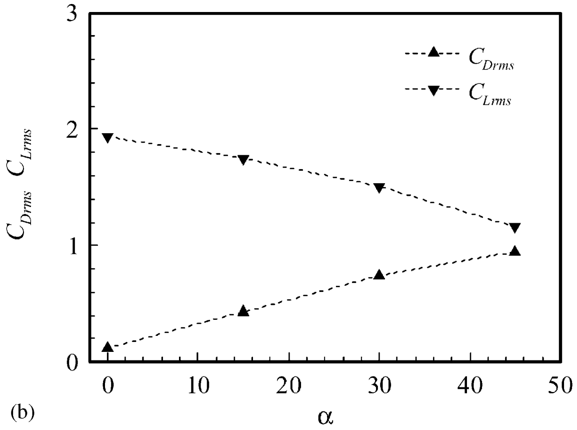

Fig. 20. Distributions of $\bar{C}_D$, $\bar{C}_L$, $C_{D\mathrm{rms}}$ and $C_{L\mathrm{rms}}$ versus α with $L = 5$ and $d = 0$: (a) $\bar{C}_D$ and $\bar{C}_L$; (b) $C_{D\mathrm{rms}}$ and $C_{L\mathrm{rms}}$.

circular cylinder impinges on the foil, according to the flow patterns and the time-dependent drag and lift coefficients acting on the foil, the preferred vortex shedding frequency of the foil is synchronized with that of the cylinder. Based on our calculated data, as expected, it is noted that the preferred vortex shedding frequency of the foil is not identical to the natural vortex shedding frequency for a uniform flow past the foil at the same incidence angle.

To demonstrate the vortex shedding frequency of the cylinder and the foil, as a typical case, Fig. 22 shows the profiles of the power spectrum density of the lift coefficients acting on the cylinder and the foil at $d = 0$, $L = 5$ and α=30° given in Fig. 4. It is noted that the highest peaks in Figs. 22(a) and (b) correspond to the same value, which is the vortex shedding frequency from the cylinder and the foil, respectively.

Fig. 23 shows the vortex shedding frequency versus L at $d = 0$ and α=30° As L increases during the range of L considered here, the frequency increases quickly and then approaches to a value of approximately 0.23 which corresponds to the natural vortex shedding frequency for uniform flow past the cylinder, as determined from the lift coefficient in Fig. 3. The behavior of the frequency varying with L may be qualitatively explained based on an analysis of linear stability theory Huerre and Monkewitz 1990, i.e., local absolute and convective stability analysis. Here, the foil in the downstream of the cylinder can be considered as a kind of approach to control the formation and shedding of vortices from the cylinder [e.g., Unal and Rockwell (1987); Kwon and Choi (1996)]. Thus, as shown in Fig. 23, the region where the frequency changes quickly (i.e., $L \leq 5$ approximately) may correspond to the absolutely unstable region behind the cylinder, and the perturbation induced by the foil can significantly influence the vortex shedding frequency of the cylinder. Meanwhile, the region where the frequency approached gradually to a constant value (i.e., $L \geq 6$ approximately) may belong to the convectively unstable region and the foil has little influence on the vortex shedding frequency of the cylinder. This behavior is consistent with the previous work performed by Unal and Rockwell (1987) and Kwon and Choi (1996).

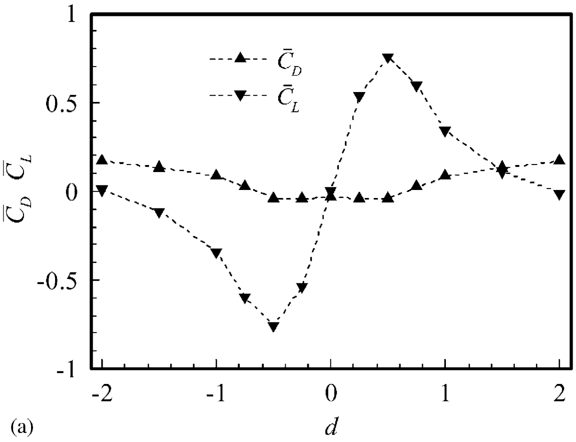

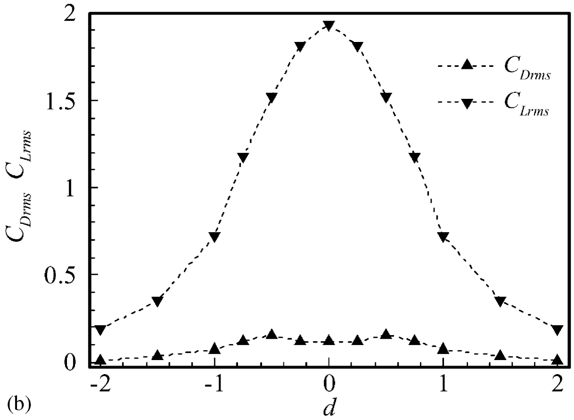

Fig. 21. Profiles of $\bar{C}_D, \bar{C}_L, C_{D\mathrm{rms}}$ and $C_{L\mathrm{rms}}$ versus d at $L = 5$ and $\alpha = 0°$: (a) $\bar{C}_D$ and $\bar{C}_L$; (b) $C_{D\mathrm{rms}}$ and $C_{L\mathrm{rms}}$.

The vortex shedding frequency with the transverse distance (d) and the incidence angle of the foil (α) is also examined. Based on our calculated results, it is noted that the change of the vortex shedding frequency in the range of $d = -2$ to 2 and $\alpha = 0°$ to $45°$ is small with respect to the change with L given in Fig. 23.

5. Concluding remarks

The vortex formation, force characteristics and vortex shedding frequency for flow around a cylinder–foil configuration, where the foil is placed in the wake of the circular cylinder, are numerically investigated by solving the two-dimensional incompressible Navier–Stokes equations with the finite element method. Based on the relative position of the foil and the cylinder, three basic types of interference are classified as the foil placed inside the cylinder wake (ICW), on the edge of the cylinder wake (ECW), and outside the cylinder wake (OCW). Some basic vortex structures, corresponding to these classifications, are identified in the near region of the foil. In view of complex flow patterns demonstrated around the foil, in particular for the classification ICW, processes of shear layer reattachment, induced separation, vortex pairing, and vortex impingement are observed. Based on the analysis for the frequency selection of the vortex shedding, it is found that a preferred vortex shedding frequency of the foil is synchronized with that of the circular cylinder. As the foil under the interaction of an incident vortex street shed from the cylinder, it is interesting to find that the mean lift and drag coefficients (i.e., $\bar{C}_D$ and $\bar{C}_L$) acting on the foil for the classification of ICW are smaller than those for the classification of OCW. Meanwhile, the mean drag and lift coefficients as well as their root-mean-square values (i.e., $C_{D\mathrm{rms}}$ and $C_{L\mathrm{rms}}$) versus the transverse distance (d), the longitudinal distance (L) and the incidence

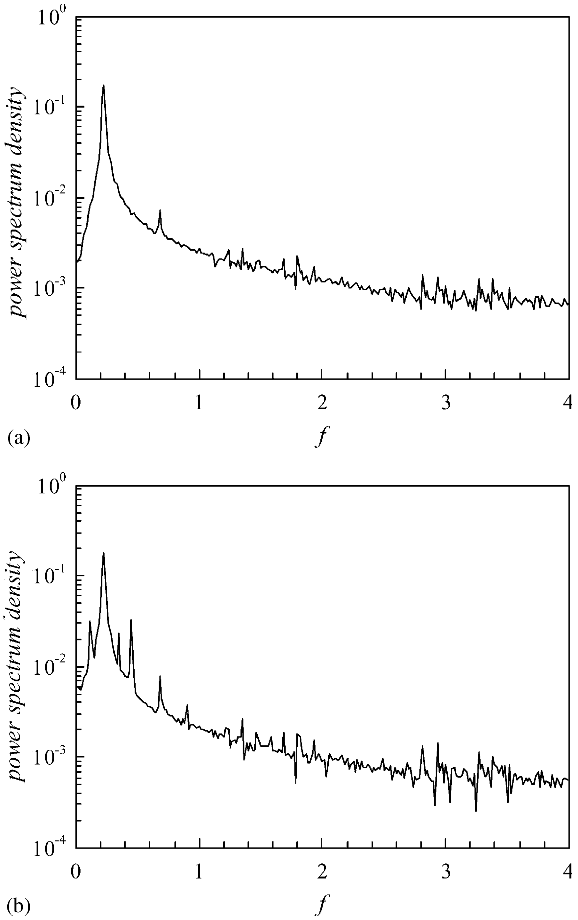

Fig. 22. Profiles of the power spectrum density (PSD) of the lift coefficients acting on the cylinder and the foil at $d = 0, L = 5$ and $\alpha = 30°$: (a) PSD of C_L on the cylinder; (b) PSD of C_L on the foil.

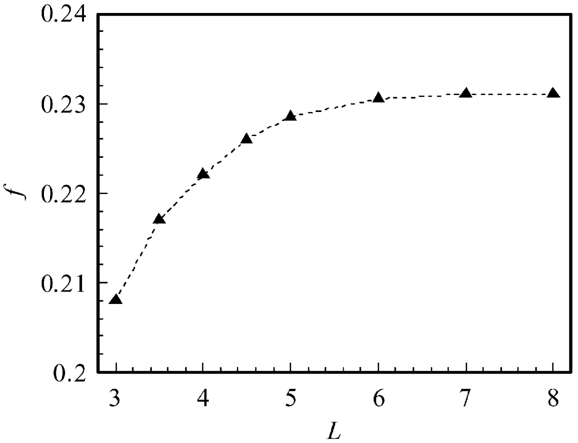

Fig. 23. Vortex shedding frequency versus L at $d = 0$ and $\alpha = 30°$.

angle of the foil (α) are investigated, respectively. These results are helpful to understand the mechanism of vortex formation, force character and vortex shedding frequency for flow past the cylinder-foil configurations.

Acknowledgements

This work was supported by the National Natural Science Foundation of China (No. 10332040, 10125210), the Innovation Project of the Chinese Academy of Sciences (No. KJCX-SW-L04, KJCX2-SW-L2), and the Programme of Hundred-Talent of the Chinese Academy of Sciences.

References

Barrett, D.S., Triantafyllou, M.S., Yue, D.K.P., Grosenbaugh, M.A., Wolfgang, M.J., 1999. Drag reduction in fish-like locomotion. Journal of Fluid Mechanics 392, 183–212.

Dalton, C., Xu, Y., Owen, J.C., 2001. The suppression of lift on a circular cylinder due to vortex shedding at moderate reynolds numbers. Journal of Fluids and Structures 15, 617–628.

Dowling, A.P., 1985. The effect of large-eddy breakup devices on oncoming vorticity. Journal of Fluid Mechanics 160, 447–463.

Gopalkrishnan, R., Triantafyllou, M.S., Triantafyllou, G.S., Barrett, D., 1994. Active vorticity control in a shear flow using a flapping foil. Journal of Fluid Mechanics 274, 1–21.

Gresho, P.M., Sani, R., 1987. On pressure boundary conditions for the incompressible Navier–Stokes equations. International Journal for Numerical Methods in Fluids 7, 1111–1145.

Gu, Z.F., Sun, T.F., 1999. On interference between two circular cylinders in staggered arrangement at high subcritical reynolds number. Journal of Wind Engineering and Industrial Engineering 80, 287–309.

Henderson, R.D., 1997. Nonlinear dynamics and pattern formulation in turbulent wake transition. Journal of Fluid Mechanics 352, 65–112.

Huerre, P., Monkewitz, P.A., 1990. Local and global instabilities in spatially developing flows. Annual Review of Fluid Mechanics 22, 473–537.

Igarashi, T., 1981. Characteristics of the flow around two circular cylinders arranged in tandem (1st report). Bulletin of the Japan Society of Mechanical Engineering 24, 323–331.

Igarashi, T., 1984. Characteristics of the flow around two circular cylinders arranged in tandem (2nd report, unique flow phenomenon at small spacing). Bulletin of the Japan Society of Mechanical Engineering 27, 2380–2387.

Kang, S., 2003. Characteristics of flow over two circular cylinders in a side-by-side arrangement at low reynolds numbers. Physics of Fluids 15, 2486–2498.

Karniadakis, G., Triantafyllou, G.S., 1989. Frequency selection and asymptotic states in laminar wakes. Journal of Fluid Mechanics 199, 441–469.

Keser, H.I., Unal, M.F., 2003. Flow around a circular cylinder downstream of a blunt-based flat plate in tandem and staggered arrangements. Journal of Fluids and Structures 17, 783–791.

Kovacs, A., Kawahara, M., 1991. A finite element scheme based on the velocity correction method for the solution of the time-dependent incompressible Navier–stokes equations. International Journal for Numerical Methods in Fluids 13, 403–423.

Kwon, K., Choi, H., 1996. Control of laminar vortex shedding behind a circular cylinder using splitter plates. Physics of Fluids 8, 479–486.

Lam, K., Cheung, W.C., 1988. Phenomena of vortex shedding and flow interference of three cylinders in different equilateral arrangements. Journal of Fluid Mechanics 196, 1–26.

Lam, K., Lo, S.C., 1992. A visualization study of cross-flow around four cylinders in a square configuration. Journal of Fluids and Structures 6, 109–131.

Lam, K., Li, J.Y., Chan, K.T., So, R.M.C., 2003. Flow pattern and velocity field distribution of cross-flow around four cylinders in a square configuration at a low reynolds number. Journal of Fluids and Structures 17, 665–679.

Lu, X.Y., 2002. Numerical study of the flow behind a rotary oscillating circular cylinder. International Journal of Computational Fluid Dynamics 16, 65–82.

Lu, X.Y., Dalton, C., 1996. Calculation of the timing of vortex formation from an oscillating cylinder. Journal of Fluids and Structures 10, 527–541.

Lu, X.Y., Sato, J., 1996. A numerical study of flow past a rotationally oscillating circular cylinder. Journal of Fluids and Structures 10, 829–849.

Lu, X.Y., Dalton, C., Zhang, J., 1997. Application of large eddy simulation to an oscillating flow past a circular cylinder. ASME Journal of Fluids Engineering 119, 519–525.

Lu, X.Y., Yang, J.M., Yin, X.Z., 2003. Propulsive performance and vortex shedding of a foil in flapping flight. Acta Mechanica 165, 189–206.

Ongoren, A., Rockwell, D., 1988. Flow structure from an oscillating cylinder. Part I, mechanisms of phase shift and recovery of the near wake. Journal of Fluid Mechanics 191, 192–223.

Persillon, H., Braza, M., 1998. Physical analysis of the transition to turbulence in the wake of a circular cylinder by three-dimensional Navier–Stokes simulation. Journal of Fluid Mechanics 365, 23–88.

Rockwell, D., 1998. Vortex-body interactions. Annual Review of Fluid Mechanics 30, 199–229.

Shen, K.Q., Dong, G.J., Lu, X.Y., 2003. The transition and instability of the shear layer in the near wake of a circular cylinder. Progress in Natural Science 13, 259–265.

Streitlien, K., Triantafyllou, G.S., Triantafyllou, M.S., 1996. Efficient foil propulsion through vortex control. AIAA Journal 34, 2315–2319.

Sumner, D., Price, S.J., Paidoussis, M.P., 2000. Flow-pattern identification for two staggered circular cylinders in cross-flow. Journal of Fluid Mechanics 411, 263–303.

Triantafyllou, M.S., Triantafyllou, G.S., Yue, D.K.P., 2000. Hydrodynamics of fishlike swimming. Annual Review of Fluid Mechanics 32, 33–53.

Unal, M.F., Rockwell, D., 1987. On vortex formation from a cylinder: part 2, control by splitter-plate interference. Journal of Fluid Mechanics 190, 513–529.

Wang, Y.X., Lu, X.Y., Zhuang, L.X., Tang, Z.M., Hu, W.R., 2004. Numerical simulation of drop marangoni migration under microgravity. Acta Aeronautica 54, 325–335.

Williamson, C.H.K., 1985. Evolution of a single wake behind a pair of bluff bodies. Journal of Fluid Mechanics 159, 1–18.

Williamson, C.H.K., 1988. The existence of two stages in the transition to three-dimensionality of a cylinder wake. Physics of Fluids 31, 3165–3168.

Williamson, C.H.K., 1996. Vortex dynamics in the cylinder wake. Annual Review of Fluid Mechanics 28, 477–539.

Williamson, C.H.K., Roshko, A., 1988. Vortex formation in the wake of an oscillating cylinder. Journal of Fluids and Structures 2, 355–381.

Wu, J.Z., Lu, X.Y., Denny, A.G., Fan, M., Wu, J.M., 1998. Post-stall flow control on an airfoil by local unsteady forcing. Journal of Fluid Mechanics 371, 21–58.

Xu, S.J., Zhou, Y., So, R.M.C., 2003. Reynolds number effects on the flow structure behind two side-by-side cylinders. Physics of Fluids 15, 1214–1219.

Zdravkovich, M.M., 1977. Review of flow interference between two circular cylinders in various arrangements. ASME Journal of Fluids Engineering 99, 618–631.

Zdravkovich, M.M., 1987. The effects of interference between circular cylinders in cross flow. Journal of Fluids and Structures 1, 239–261.

Zhou, Y., Wang, Z.J., So, R.M.C., Xu, S.J., Jin, W., 2001. Free vibrations of two side-by-side cylinders in a cross flow. Journal of Fluid Mechanics 443, 197–229.

Zhou, Y., Zhang, H.J., Yiu, M.W., 2002. The turbulent wake of two side-by-side circular cylinders. Journal of Fluid Mechanics 458, 303–332.